# Supersonic and Hypersonic Flows on 2D Unstructured Context: Part III

Edisson S. G. Maciel and Nikos E. Mastorakis

***Abstract*—**In this work, the third of this study, numerical simulations involving supersonic and hypersonic flows on an unstructured context are analyzed. The Van Leer and the Radespiel and Kroll schemes are implemented on a finite volume formulation, using unstructured spatial discretization. The algorithms are implemented in their first and second order spatial accuracies. The second order spatial accuracy is obtained by a linear reconstruction procedure based on the work of Barth and Jespersen. Several non-linear limiters are studied using the linear interpolation based on the work of Jacon and Knight. To the turbulent simulations, the Wilcox, the Menter and Rumsey and the Yoder, Georgiadids and Orkwis models are employed. The compression corner problem to the supersonic inviscid simulations and the re-entry capsule problem to the hypersonic viscous simulations are studied. The results have demonstrated that the Van Leer algorithm yields the best results in terms of the prediction of the shock angle of the oblique shock wave in the compression corner problem and the best value of the stagnation pressure at the configuration nose in the re-entry capsule configuration. The spatially variable time step is the best choice to accelerate the convergence of the numerical schemes, as reported by Maciel. In terms of turbulent results, the Wilcox model yields the best results, proving the good capacity of this turbulence model in simulate high hypersonic flows. This paper is continuation of Maciel's works started in 2011 and treats mainly the influence of turbulence models on the solution quality.

***Keywords*—** Euler and Navier-Stokes equations; Menter and Rumsey turbulence model; Radespiel and Kroll algorithm; Unstructured spatial discretization; Van Leer algorithm; Wilcox turbulence model; Yoder, Georgiadids and Orkwis turbulence model.

## I. Introduction

CONVENTIONAL non-upwind algorithms have been used extensively to solve a wide variety of problems ([1]). Conventional algorithms are somewhat unreliable in the sense that for every different problem (and sometimes, every different case in the same class of problems) artificial dissipation terms must be specially tuned and judicially chosen for convergence. Also, complex problems with shocks and steep compression and expansion gradients may defy solution altogether.

Upwind schemes are in general more robust but are also more involved in their derivation and application. Some upwind schemes that have been applied to the Euler equations are, for example, [2-4]. Some comments about these methods are reported below:

[2] suggested an upwind scheme based on the flux vector splitting concept. This scheme considered the fact that the convective flux vector components could be written as flow Mach number polynomial functions, as main characteristic. Such polynomials presented the particularity of having the minor possible degree and the scheme had to satisfy seven basic properties to form such polynomials. This scheme was presented to the Euler equations in Cartesian coordinates and three-dimensions.

[3] proposed a new flux vector splitting scheme. They declared that their scheme was simple and its accuracy was equivalent and, in some cases, better than the [5] scheme accuracy in the solutions of the Euler and the Navier-Stokes equations. The scheme was robust and converged solutions were obtained so fast as the [5] scheme. The authors proposed the approximated definition of an advection Mach number at the cell face, using its neighbor cell values via associated characteristic velocities. This interface Mach number was so used to determine the upwind extrapolation of the convective quantities.

[4] emphasized that the [3] scheme had its merits of low computational complexity and low numerical diffusion as compared to other methods. They also mentioned that the original method had several deficiencies. The method yielded local pressure oscillations in the shock wave proximities, adverse mesh and flow alignment problems. In the [4] work, a hybrid flux vector splitting scheme, which alternated between the [3] scheme and the [2] scheme, in the shock wave regions, was proposed, assuring that resolution of strength shocks was clear and sharply defined.

The motivation of the present study is described in [6,7] and the interesting reader is encouraged to read this reference to become familiar with the equations and its applications.

In this work, the third of this study, numerical simulations involving supersonic and hypersonic flows on an unstructured context are analysed. The [2, 4] schemes are implemented on a finite volume formulation, using unstructured spatial discretization. The algorithms are implemented in their first and second order spatial accuracies. The second order spatial

Edisson S. G. Maciel is witht the Federal University of Great Dourados, Rodovia Dourados – Itahum, km 12 – Caixa Postal 364 – Dourados, MS, Brazil – 79804-970 (corresponding author, phone number: +55 012 99174-3844; e-mail: edisavio@edissonsavio.eng.br).

Nikos E. Mastorakis is with WSEAS (World Scientific and Engineering Academy and Society), A. I. Theologou 17-23, 15773 Zografou, Athens, Greece, E-mail: mastor@wseas.org as well as with the Technical University of Sofia, Industrial Engineering Department, Sofia, 1000, Bulgaria mailto:mastor@tu-sofia.bg

accuracy is obtained by a linear reconstruction procedure based on the work of [8]. Several non-linear limiters are studied using the linear interpolation based on the work of [9]. To the turbulent simulations, the [10-12] models are employed. The compression corner problem to the inviscid simulations and the re-entry capsule problem to the hypersonic viscous simulations are studied. The results have demonstrated that the [2] algorithm yields the best results in terms of the prediction of the shock angle of the oblique shock wave in the compression corner problem and the best value of the stagnation pressure at the configuration nose in the re-entry capsule configuration. The spatially variable time step is the best choice to accelerate the convergence of the numerical schemes, as reported by [13-14]. In terms of turbulent results, the [10] model yields the best results, proving the good capacity of this turbulence model in simulate high hypersonic flows. This paper is continuation of Maciel's works started in 2011 and treats mainly the influence of turbulence models on the solution quality.

## II. Navier-Stokes Equations and Algorithms

The Navier-Stokes equations, defined by the two-equation turbulence models treated herein, are presented in details in [6], and are not repeated here. The interesting reader is encouraged to read [6].

The employed algorithms in this study are also described in [6], as also the linear reconstruction procedure to obtain high resolution of [9], and are not repeated herein.

## III. Wilcox Turbulence Model

In this work, the k-ω model of [10] is one of the studied models, where s = ω (s is the second turbulent variable). To define the turbulent viscosity in terms of k and ω, one has:

$$\mu_T = \mathrm{Re}\,\rho k/\omega. \qquad (1)$$

where: k is the turbulent kinetic energy, ω is the vorticity, ρ is the fluid density, Re is the Reynolds number, and μT is the turbulent viscosity.

The source term denoted by G in the governing equation contains the production and dissipation terms of k and ω. To the [10] model, the $G_k$ and $G_\omega$ terms have the following expressions:

$$G_k = -P_k + D_k \quad \text{and} \quad G_\omega = -P_\omega + D_\omega, \qquad (2)$$

where:

$$P_k = \mu_T\left(\frac{\partial u}{\partial y} + \frac{\partial v}{\partial x}\right)\frac{\partial u}{\partial y}, \quad D_k = \beta^*\rho\omega k/\mathrm{Re};$$

$$P_\omega = \alpha_\omega \omega/k P_k, \text{ and } D_\omega = \beta\rho\omega^2/\mathrm{Re}. \qquad (3)$$

The closure coefficients adopted to the [10] model assume the following values: $\alpha_\omega = 5/9$; $\beta = 3/40$; $\beta^* = 0.09$; $\sigma_k = 2.0$; $\sigma_\omega = 2.0$; $Prd_L = 0.72$; $Prd_T = 0.9$.

## IV. Menter and Rumsey Turbulence Model

The [11] model presents four variants: k-ω model of Wilcox, k-ε of two layers, BSL model of [15], and SST (Shear Stress Transport) model of [15]. They are defined as follows:

### A. k-ω model of Wilcox

Constants of the k-ω model of [10]:

$\beta_1^* = 0.09$, $\sigma_1^* = 0.5$, $\kappa_1 = 0.41$, $\gamma_1 = 5/9$, $\sigma_1 = 0.5$ and $\beta_1 = \left(\gamma_1 + \sigma_1\kappa_1^2/\sqrt{\beta_1^*}\right)\beta_1^*$;

Constants of the standard k-ε model of [16]:

$C_\mu = 0.09$, $C_{\varepsilon 1} = 1.44$, $C_{\varepsilon 2} = 1.92$, $\sigma_k$ = 1.0, and $\sigma_\varepsilon$ = 1.17;

Constants of the equivalent k-ε model:

$\beta_2^* = C_\mu$, $\sigma_2^* = 1/\sigma_k$, $\kappa_2 = 0.41$, $\gamma_2 = C_{\varepsilon 1} - 1.0$, $\sigma_2 = 1/\sigma_\varepsilon$, and $\beta_2 = (C_{\varepsilon 2} - 1.0)C_\mu$;

Weighting function, $F_1$:

$F_1$ = 1.0;

Turbulent viscosity:

$\mu_T = \mathrm{Re}\,\rho k/\omega$;

### B. k-ε model of two layers

Constants of the k-ω model of [10]:

$\beta_1^* = 0.09$, $\sigma_1^* = 0.5$, $\kappa_1 = 0.41$, $\gamma_1 = 5/9$, $\sigma_1 = 0.4$ and $\beta_1 = \left(\gamma_1 + \sigma_1\kappa_1^2/\sqrt{\beta_1^*}\right)\beta_1^*$;

Constants of the equivalent k-ε model:

$\beta_2^* = 0.09$, $\sigma_2^* = 1.0$, $\kappa_2 = 0.41$, $\gamma_2$ = 0.44, $\sigma_2 = 0.857$, and $\beta_2 = \left(\gamma_2 + \sigma_2\kappa_2^2/\sqrt{\beta_2^*}\right)\beta_2^*$;

Weighting function, $F_1$:

$\Gamma_1$ parameter:

$$\Gamma_1 = 500\upsilon_M/\left(n^2\omega\right), \qquad (4)$$

with: $\upsilon_M = \mu_M / \rho$ and n = normal distance from the wall to the cell under study;

Coefficient $CD_{k-\omega}$:

$$CD_{k-\omega} = MAX\left[\left(2\rho\sigma_2 / \omega \frac{\partial k}{\partial y}\frac{\partial \omega}{\partial y}\right) \Big/ Re,\ 10^{-20}\right]; \quad (5)$$

$\Gamma_2$ parameter:

$$\Gamma_2 = 4\rho\sigma_2 k / \left(n^2 CD_{k-\omega}\right); \quad (6)$$

$\Gamma_M$ parameter:

$$\Gamma_M = MIN\left(\Gamma_1, \Gamma_2\right); \quad (7)$$

$$F_1 = TANH\left(\Gamma_M^4\right); \quad (8)$$

Turbulent viscosity:

$$\mu_T = Re\,\rho k / \omega;$$

*C. Menter's BSL model*

Constants of the k-ω model of [10]:

$\beta_1^* = 0.09$, $\sigma_1^* = 0.5$, $\kappa_1 = 0.41$, $\gamma_1 = 5/9$, $\sigma_1 = 0.5$ and $\beta_1 = \left(\gamma_1 + \sigma_1\kappa_1^2 / \sqrt{\beta_1^*}\right)\beta_1^*$;

Constants of the equivalent k-ε model:

$\beta_2^* = 0.09$, $\sigma_2^* = 1.0$, $\kappa_2 = 0.41$, $\gamma_2 = 0.44$, $\sigma_2 = 0.857$, and $\beta_2 = \left(\gamma_2 + \sigma_2\kappa_2^2 / \sqrt{\beta_2^*}\right)\beta_2^*$;

Weighting function, $F_1$:

$\Gamma_1$ parameter:

$\Gamma_1 = 500\upsilon_M / \left(n^2\omega\right)$;

Coefficient CDk-ω:

$$CD_{k-\omega} = MAX\left[\left(2\rho\sigma_2 / \omega \frac{\partial k}{\partial y}\frac{\partial \omega}{\partial y}\right) \Big/ Re,\ 10^{-20}\right];$$

$\Gamma_2$ parameter:

$$\Gamma_2 = 4\rho\sigma_2 k / \left(n^2 CD_{k-\omega}\right);$$

$\Gamma_3$ parameter:

$$\Gamma_3 = \sqrt{k} / \left(\beta_1^* \omega n\right); \quad (9)$$

$\Gamma_M$ parameter:

$$\Gamma_M = MIN\left[MAX\left(\Gamma_1, \Gamma_3\right), \Gamma_2\right]; \quad (10)$$

$$F_1 = TANH\left(\Gamma_M^4\right);$$

Turbulent viscosity:

$$\mu_T = \rho k / \omega\, Re;$$

*D. Menter's SST model*

Constants of the k-ω model of [10]:

$\beta_1^* = 0.09$, $\sigma_1^* = 0.5$, $\kappa_1 = 0.41$, $\gamma_1 = 5/9$, $\sigma_1 = 0.5$ and $\beta_1 = \left(\gamma_1 + \sigma_1\kappa_1^2 / \sqrt{\beta_1^*}\right)\beta_1^*$;

Constants of the equivalent k-ε model:

$\beta_2^* = 0.09$, $\sigma_2^* = 1.0$, $\kappa_2 = 0.41$, $\gamma_2 = 0.44$, $\sigma_2 = 0.857$, and $\beta_2 = \left(\gamma_2 + \sigma_2\kappa_2^2 / \sqrt{\beta_2^*}\right)\beta_2^*$;

Weighting function, $F_1$:

$\Gamma_1$ parameter:

$\Gamma_1 = 500\upsilon_M / \left(n^2\omega\right)$;

Coefficient CDk-ω:

$$CD_{k-\omega} = MAX\left[\left(2\rho\sigma_2 / \omega \frac{\partial k}{\partial y}\frac{\partial \omega}{\partial y}\right) \Big/ Re,\ 10^{-20}\right];$$

$\Gamma_2$ parameter:

$\Gamma_2 = 4\rho\sigma_2 k / \left(n^2 CD_{k-\omega}\right)$;

$\Gamma_3$ parameter:

$\Gamma_3 = \sqrt{k} / \left(\beta_1^* \omega n\right)$;

$\Gamma_M$ parameter:

$\Gamma_M = MIN\left[MAX\left(\Gamma_1, \Gamma_3\right), \Gamma_2\right]$;

$F_1 = TANH\left(\Gamma_M^4\right)$;

Weighting function, $F_2$:

$\Gamma_M$ parameter:

$$\Gamma_M = \mathrm{MIN}(2\Gamma_3, \Gamma_1); \quad (11)$$

$$F_2 = \mathrm{TANH}(\Gamma_M^2); \quad (12)$$

$\Omega$ parameter:

$$\Omega = |\partial u/\partial y|; \quad (13)$$

Turbulent viscosity:

$$\mu_T = \rho \mathrm{MIN}[k/\omega, a_1 k/(\Omega F_2)]\mathrm{Re}, \quad (14)$$

where a1 = 0.31.

With these definitions, each model can determine the following additional constants:

$$\sigma^* = \sigma_1^* F_1 + (1-F_1)\sigma_2^*; \quad (15)$$
$$\sigma = \sigma_1 F_1 + (1-F_1)\sigma_2; \quad (16)$$
$$\sigma_k = 1/\sigma^* \quad \text{and} \quad \sigma_\omega = 1/\sigma; \quad (17)$$
$$\gamma = \gamma_1 F_1 + (1-F_1)\gamma_2; \quad (18)$$
$$\beta = \beta_1 F_1 + (1-F_1)\beta_2; \quad (19)$$
$$\beta^* = \beta_1^* F_1 + (1-F_1)\beta_2^*. \quad (20)$$

The source term denoted by G in the governing equation contains the production and dissipation terms of k and ω. To the [11] model, the $G_k$ and $G_\omega$ terms have the following expressions:

$$G_k = -P_k + D_k \quad \text{and} \quad G_\omega = -P_\omega + D_\omega - \mathrm{Dif}_\omega, \quad (21)$$

where:

$$P_k = \mu_T\left(\frac{\partial u}{\partial y} + \frac{\partial v}{\partial x}\right)\frac{\partial u}{\partial y};\ D_k = \beta^*\rho k\omega/\mathrm{Re};$$
$$P_\omega = \gamma P_k/\upsilon_T;\ D_\omega = \beta\rho\omega^2/\mathrm{Re};$$
$$\mathrm{Dif}_\omega = (1-F_1)\frac{2\rho\sigma_2}{\omega}\frac{\partial k}{\partial y}\frac{\partial \omega}{\partial y}\Big/\mathrm{Re}, \quad (22)$$

with: $\upsilon_T = \mu_T/\rho$.

## V. YODER, GEORGIADIDS AND ORKWIS

The [12] turbulence model adopts the following closure coefficients: $R_s = 8.0$, $R_k = 6.0$, $R_\omega = 2.7$, $\xi_k = 1.0$, $\xi_\omega = 0.0$, $\beta = 3/40$, $M_{T,0} = 0.0$, $\alpha_0 = 0.1$, $\alpha_0^* = \beta/3$, $\sigma_k = 2.0$ and $\sigma_\omega = 2.0$. The turbulent Reynolds number is specified by:

$$\mathrm{Re}_T = \rho k/(\mu_M \omega). \quad (23)$$

The parameter α* is given by:

$$\alpha^* = (\alpha_0^* + \mathrm{Re}_T/R_k)/(1+\mathrm{Re}_T/R_k). \quad (24)$$

The turbulent viscosity is specified by:

$$\mu_T = \mathrm{Re}\,\alpha^*\rho k/\omega. \quad (25)$$

The source term denoted by G in the governing equation contains the production and dissipation terms of k and ω. To the [12] model, the $G_k$ and $G_\omega$ terms have the following expressions:

$$G_k = -P_k + D_k \quad \text{and} \quad G_\omega = -P_\omega + D_\omega,$$

where:

$P_k$ is given by Eq. (3).

The turbulent Mach number is defined as:

$$M_T = \sqrt{2k/a^2}. \quad (26)$$

It is also necessary to specify the function F:

$$F = \mathrm{MAX}(M_T^2 - M_{T,0}^2, 0.0). \quad (27)$$

The $\beta^*$ parameter is given by:

$$\beta^* = 0.09\left[5/18 + (\mathrm{Re}_T/R_S)^4\right]/\left[1+(\mathrm{Re}_T/R_S)^4\right] \quad (28)$$

and the dissipation term of turbulent kinetic energy is obtained:

$$D_k = \beta^*\rho\omega k(1+\xi_k F)/\mathrm{Re}; \quad (29)$$

The production term of vorticity is defined by:

$$P_\omega = \alpha\omega/kP_k, \quad (30)$$

with:

$$\alpha = 5/9(\alpha_0 + \mathrm{Re}_T/R_\omega)(1+\mathrm{Re}_T/R_\omega)/\alpha^*. \quad (31)$$

Finally, the vorticity dissipation term is determined by:

$$D_\omega = \rho\omega^2(\beta + \beta^*\xi_\omega F)/\mathrm{Re}. \quad (32)$$

## VI. UNSTRUCTURED TRIANGULATION

An unstructured discretization of the calculation domain is usually recommended to complex configurations, due to the easily and efficiency that such domains can be discretized ([17-19]). However, the unstructured mesh generation question will not be studied in this work. The unstructured meshes generated in this work were structured created and posteriorly the connectivity, neighboring, node coordinates and ghost tables were built in a pre-processing stage.

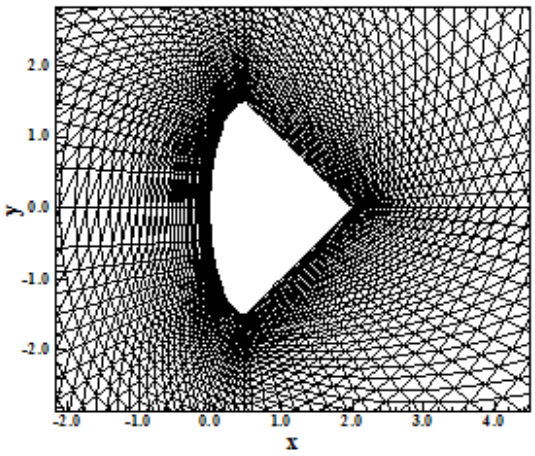


Figure 1. Triangulation in the Same Sense (SS).

A study involving two types of domain triangulation is performed. In the first case, the mesh is generated with the triangles created in the same sense (see Fig. 1). In the second case, the triangles generated in one row is in a specific sense and in the above row is in an opposite sense (see Fig. 2), originating a mesh with more regular geometrical properties. It is important to emphasize that in the second method, the number of lines should be odd. These triangulation options are studied in the inviscid and turbulent cases. As in [6-7] the alternated generation provides excellent results in symmetrical configurations. It is expected to be repeated in this study.

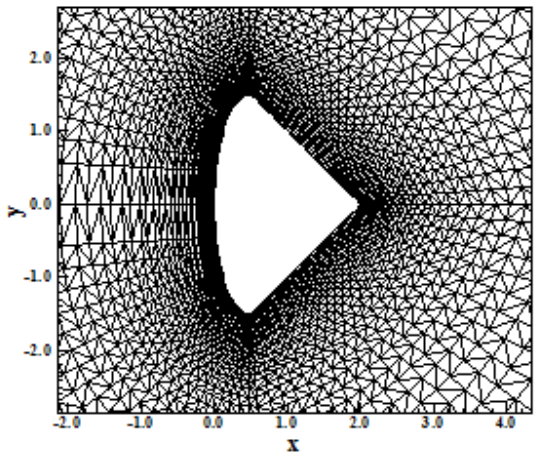


Figure 2. Triangulation in Alternate Sense (AS).

## VII. TIME STEP

As in [6-7] the spatially variable time step procedure resulted in an excellent tool to accelerate convergence, it is repeated in this study with the expectative of also improve the convergence rate of the numerical schemes. For details of such implementation the reader is encouraged to read [6], as for the convective case as for the convective + diffusive case.

## VIII. INITIAL AND BOUNDARY CONDITIONS

Freestream values, at all grid cells, are adopted for all flow properties as initial condition, as suggested by [17,20]. This initial condition is specified in [6].

The boundary conditions are basically of five types: solid wall, entrance, exit, far field and continuity. These conditions are implemented with the help of ghost cells and details of such implementation are also described in [6].

## IX. RESULTS

Simulations were performed using a personal notebook with processor INTEL core i7 and 8GBytes of RAM memory. The convergence criterion consisted of a reduction of four (4) orders in the magnitude of the residual. The residual was defined as the maximum value of the discretized equations. As one have four (4) equations to the inviscid case and six (6) equations to the turbulent case, each one should be tested to obtain the value of the maximum discretized equation for each cell. Comparing all discretization equation values, one obtains the maximum residual in the field. The entrance or attack angle in the present simulations was adopted equal to 0.0o. The value of $\gamma$ was estimated in 1.4 for "cold gas" flow simulations. Two problems were studied: the compression corner (inviscid case) and the reentry capsule (turbulent case).

### *A. Inviscid Solutions – Same Sense Mesh Generation*

In the inviscid case, it was studied the supersonic flow along a compression corner with $10^o$ of inclination angle. The freestream Mach number was adopted equal to 3.0, a moderate supersonic flow. The compression corner configuration and the corner mesh are show in Figs. 3 and 4. Details of the same sense (SS) and alternated sense (AS) mesh generations are presented in Figs. 5 and 6. This mesh is composed of 6,900 triangular cells and 3,570 nodes, which corresponds to a mesh of 70x51 points in a finite difference context.

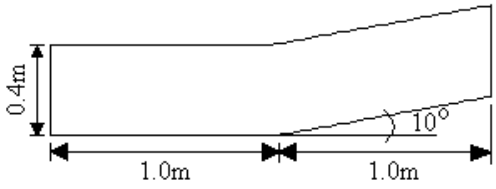


Figure 3. Compression corner configuration.

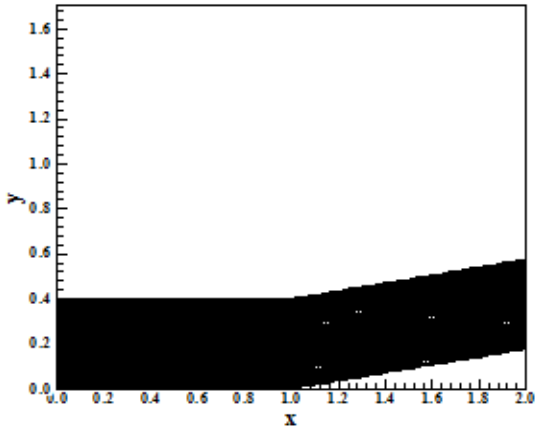


Figure 4. Compression corner mesh (70x51).

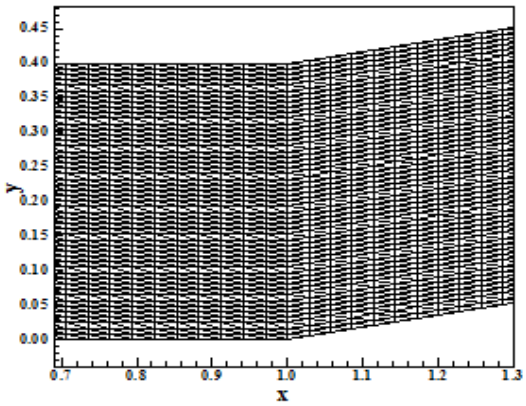


Figure 5. Detail of the SS mesh generation.

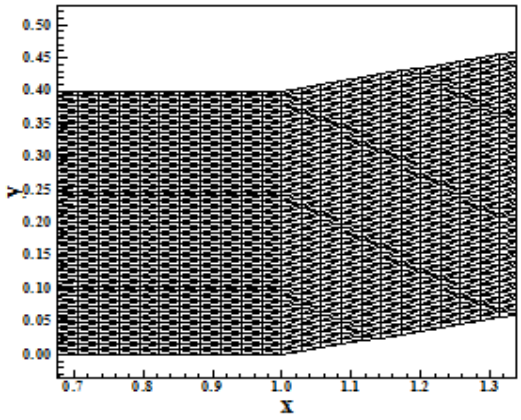


Figure 6. Details of the AS mesh generation.

Figures 7 to 11 exhibit the pressure contours obtained by the [2] scheme, in its five variants, to a second order high resolution solution. The five variants were abbreviated as follows: Barth and Jespersen (BJ), Van Leer (VL), Van Albada (VA), Super Bee (SB) and β-limiter (BL). All variants of the [2] algorithm capture appropriately the shock wave at the corner. Oscillations are not present, which indicates that the wall pressure distribution of each variant is smooth and well defined.

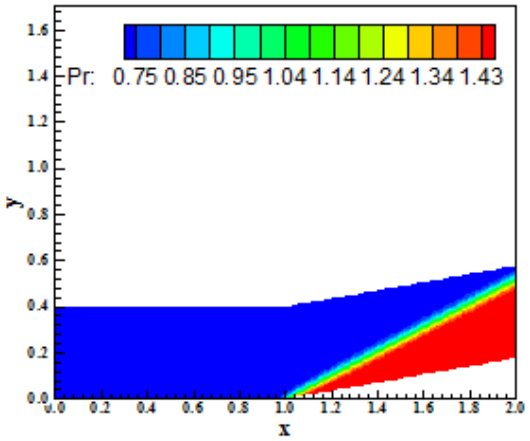


Figure 7. Pressure contours (VL-BJ).

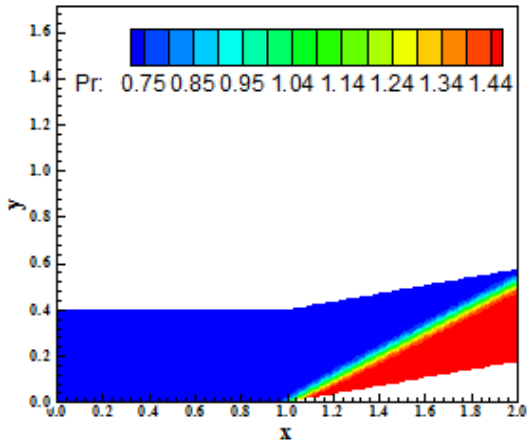


Figure 8. Pressure contours (VL-VL).

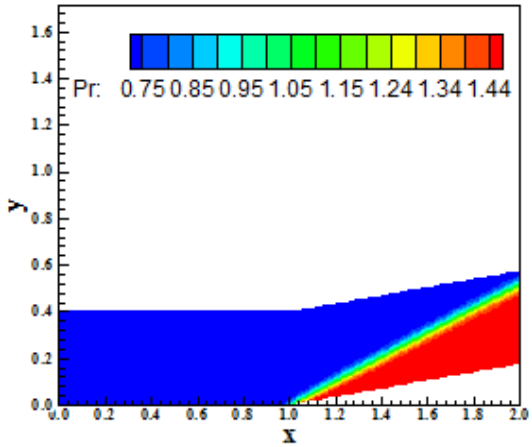


Figure 9. Pressure contours (VL-VA).

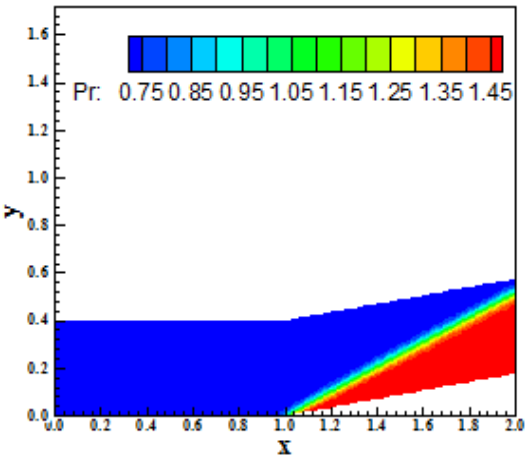


Figure 10. Pressure contours (VL-SB).

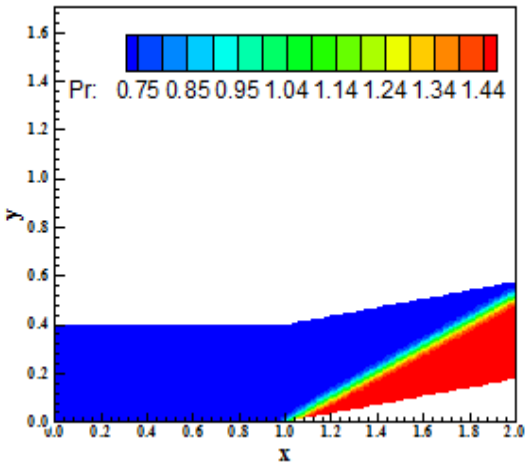


Figure 11. Pressure contours (VL-BL).

In the second order solutions with the [2] algorithm none of the variants present differences in terms of thickness width, which is expected to the SB limiter, due to its improved capability of capturing shock waves, as reported by [21].

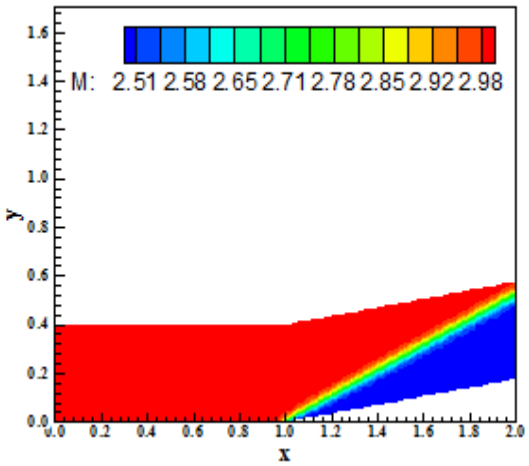


Figure 12. Mach number contours (VL-BJ).

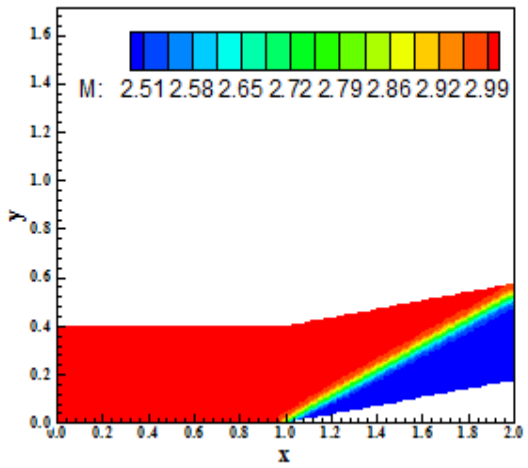


Figure 13. Mach number contours (VL-VL).

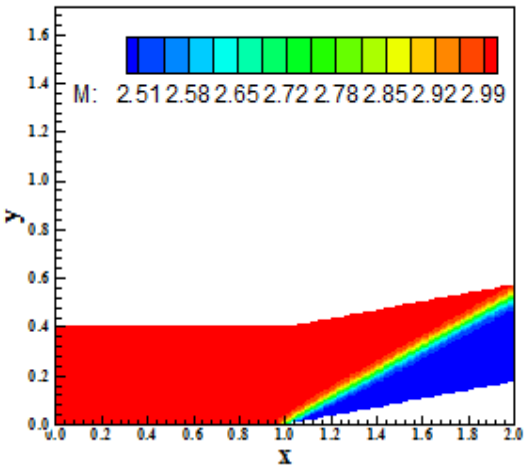


Figure 14. Mach number contours (VL-VA).

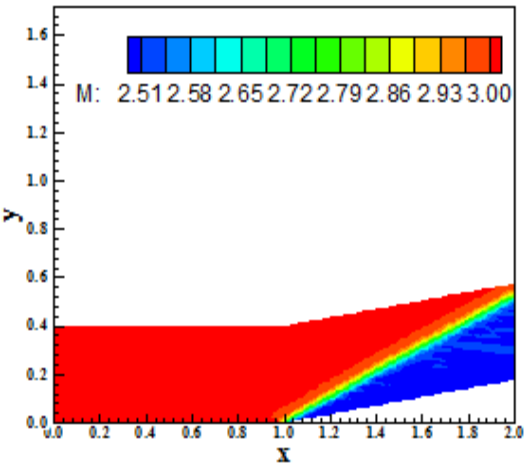


Figure 15. Mach number contours (VL-SB).

Figures 12 to 16 present the Mach number contours obtained by each variant of the [2] algorithm. The solutions are, in general, of good quality, but some oscillations appear in

the SB and BL results. The shock wave is well captured by the variants of the [2] algorithm in the Mach number contours results too.

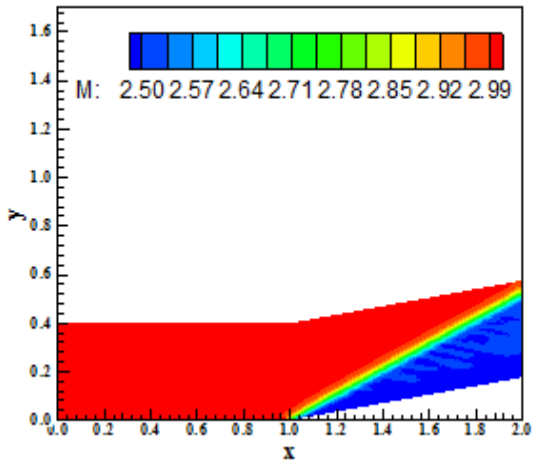


Figure 16. Mach number contours (VL-BL).

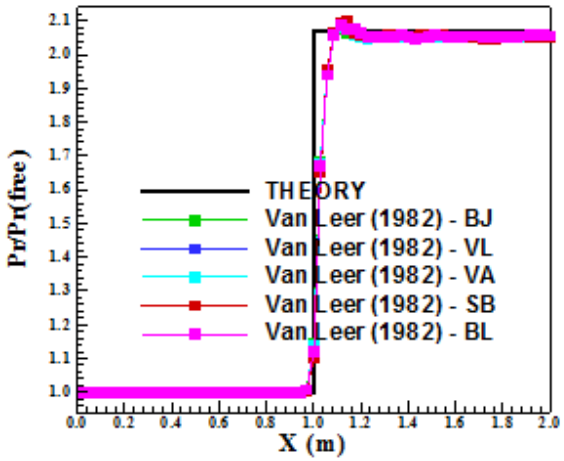


Figure 17. Wall pressure distributions (VL).

Figure 17 shows the wall pressure distributions of each variant of the [2] scheme. They are compared with the oblique shock wave theory results. They are plotted with symbols to illustrate how many points are necessary to capture the discontinuity. As can be observed, all solutions capture the shock discontinuity with four (4) cells. The best wall pressure distributions are due to BJ and VL non-linear limiters. The other limiters present a pressure peak at the discontinuity region, which damages its solution quality.

One way to quantitatively verify if the solutions generated by each scheme are satisfactory consists in determining the shock angle of the oblique shock wave, β, measured in relation to the initial direction of the flow field. [22] (pages 352 and 353) presents a diagram with values of the shock angle, β, to oblique shock waves. The value of this angle is determined as function of the freestream Mach number and of the deflection angle of the flow after the shock wave, ϕ. To $\phi = 10^{o}$ (corner inclination angle) and to a freestream Mach number equals to 3.0, it is possible to obtain from this diagram a value to β equals to 27.5º. Using a transfer in Figures 7 to 11, it is possible to obtain the values of β to each scheme, as well the respective errors, shown in Tab. 1. The results highlight the [2] scheme, in its SB variant, as the most accurate of the studied versions, with error of 0.00%.

Table 1. Shock angle and percentage errors ([2]).

| Variant | β (°) | Error (%) |
|---|---|---|
| BJ | 28.0 | 1.82 |
| VL | 27.9 | 1.45 |
| VA | 28.0 | 1.82 |
| SB | 27.5 | 0.00 |
| BL | 27.6 | 0.36 |

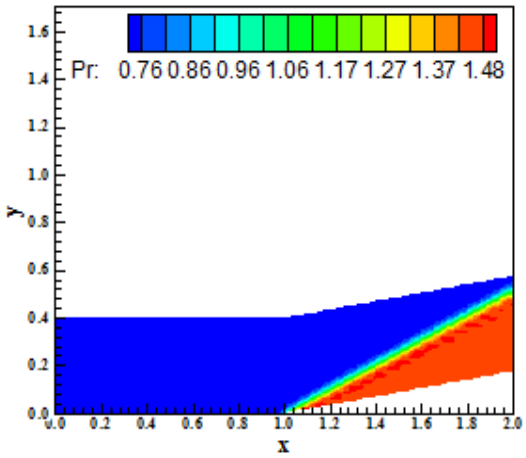


Figure 18. Pressure contours (RK-BJ).

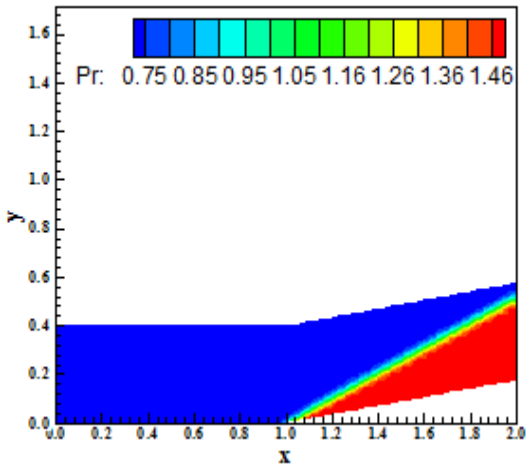


Figure 19. Pressure contours (RK-VL).

Figures 18 to 22 exhibit the pressure contours obtained with the [4] scheme, in its five variants. All figures present pressure oscillations. The reasonable solution is that generated by the VL variant. From the analysis aforementioned, it is reasonable to predict pressure oscillation at the wall pressure

distributions.

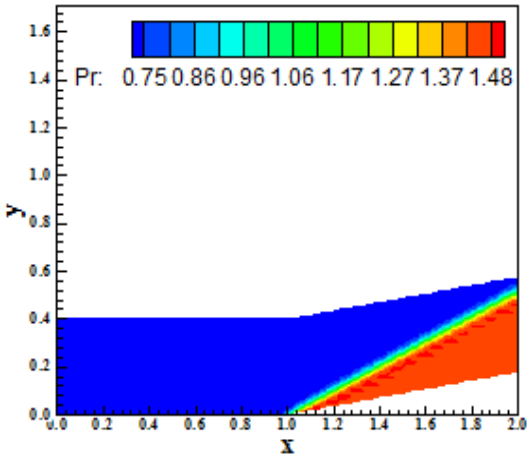


Figure 20. Pressure contours (RK-VA).

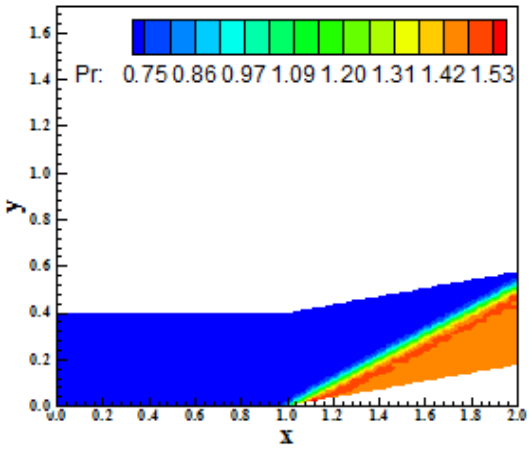


Figure 21. Pressure contours (RK-SB).

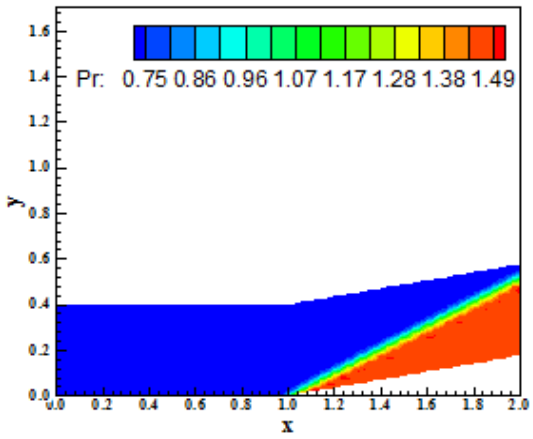


Figure 22. Pressure contours (RK-BL).

The oscillations are more significant in the SB solution. Figures 23 to 27 show the Mach number contours obtained with the [4] algorithm in its five versions. All solutions present oscillations. The reasonable solution is that presented by the BL variant.

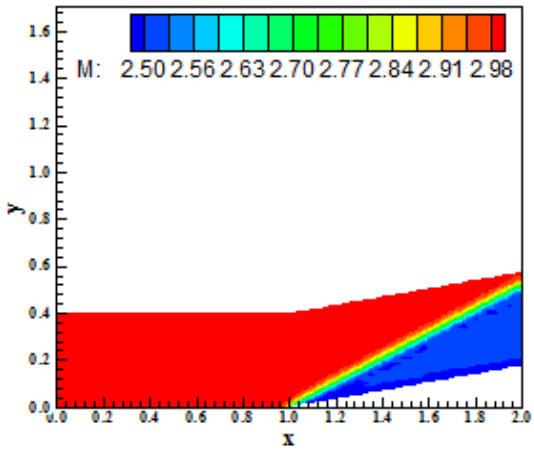


Figure 23. Mach number contours (RK-BJ).

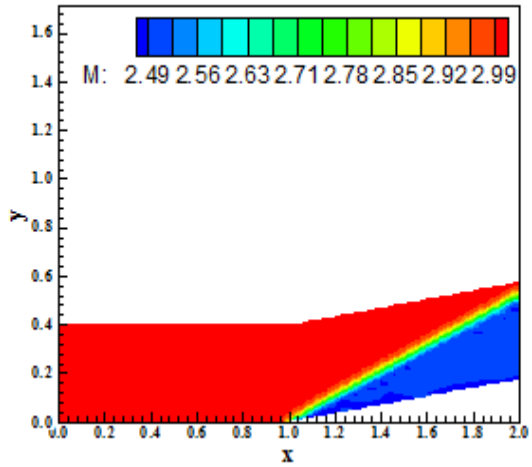


Figure 24. Mach number contours (RK-VL).

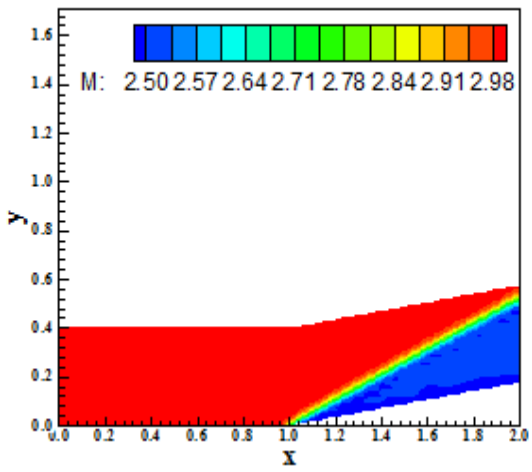


Figure 25. Mach number contours (RK-VA).

Figure 28 presents the wall pressure distributions obtained by the [4] algorithm in their five versions. The solutions are compared with the oblique shock wave theory results. All

algorithms capture the discontinuity in five cells, characterizing this scheme as worse than the [2] scheme, to the SS mesh generation. The pressure peak is present in all solutions and the VL variant is the most reasonable result that can be considered for comparison.

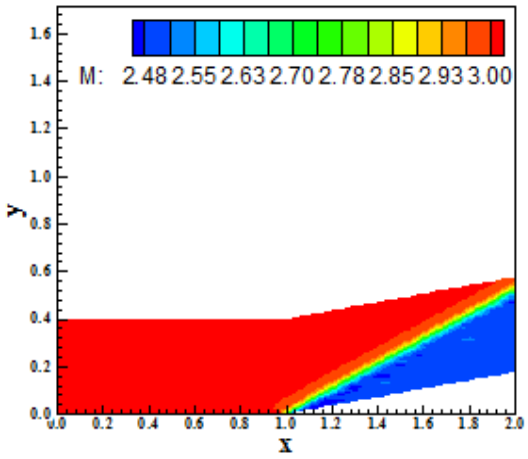


Figure 26. Mach number contours (RK-SB).

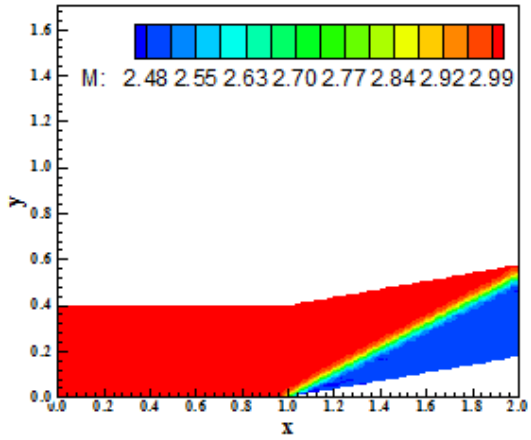


Figure 27. Mach number contours (RK-BL).

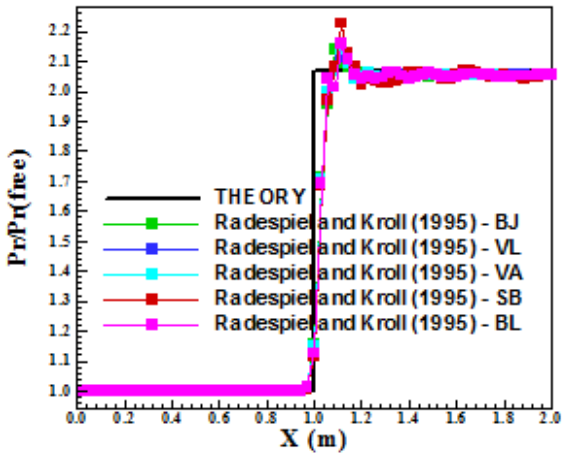


Figure 28. Wall pressure distributions (RK).

Again, the shock angle of the oblique shock wave can be considered to quantitatively measure the level of accuracy that each variant of the [4] scheme presents for. Noting that again $\beta_{THEORETICAL} = 27.5°$, using a transfer in Figs. 18 to 22, one has in Tab. 2:

Table 2. Shock angle and percentage errors ([4]).

| Variant | β (°) | Error (%) |
|---|---|---|
| BJ | 27.4 | 0.36 |
| VL | 27.4 | 0.36 |
| VA | 28.0 | 1.82 |
| SB | 27.4 | 0.36 |
| BL | 27.5 | 0.00 |

The results highlight the [4] scheme, in its BL variant, as the most accurate of the studied versions. The percentage error was 0.00%.

### *B. Inviscid Solutions – Alternated Sense Mesh Generation*

To the alternated sense mesh generation, the same problem was studied. A freestream Mach number of 3.0 (moderate supersonic flow) was used to perform the numerical simulation. This is the equal condition used in the same sense mesh generation study.

Figures 29 to 33 show the pressure contours obtained by the [2] algorithm in its five versions. It is a remarkable aspect of these solutions that the thickness of the shock wave is very thin as compared to the same results of the SS case. All solutions present this aspect and their quality is significantly improved. Moreover, the shock wave is well captured by the [2] scheme in its variants.

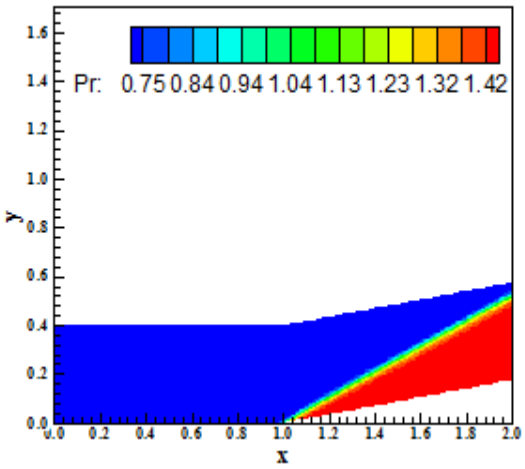


Figure 29. Pressure contours (VL-BJ).

Figures 34 to 38 exhibit the Mach number contours obtained by the [2] scheme in its variants. The main feature of reducing the thickness of the shock wave is again repeated. Although the SB and BL present oscillations in their solutions, which originates non-homogeneity in the Mach number contours, the

thickness is still thin. All variants capture appropriately the shock wave.

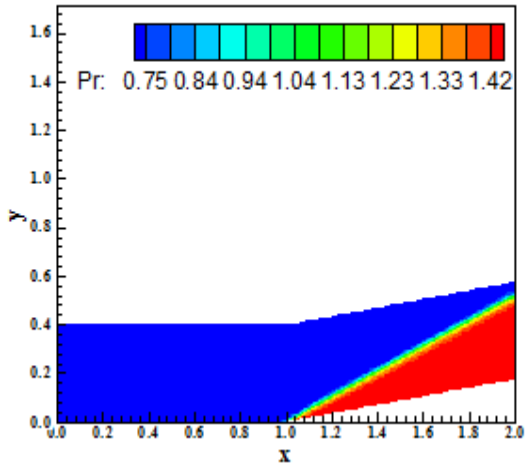


Figure 30. Pressure contours (VL-VL).

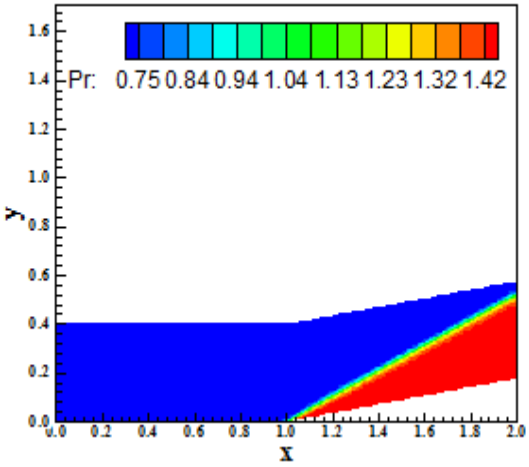


Figure 31. Pressure contours (VL-VA).

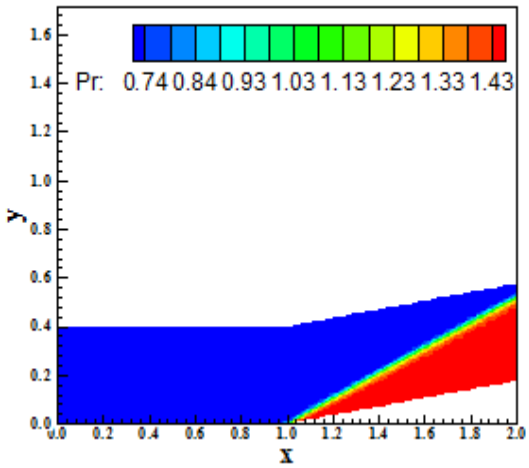


Figure 32. Pressure contours (VL-SB).

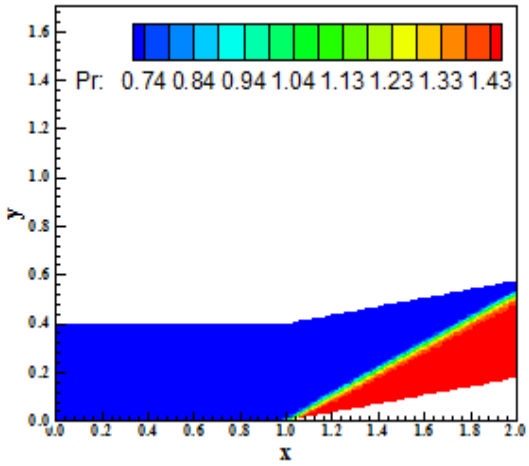


Figure 33. Pressure contours (VL-BL).

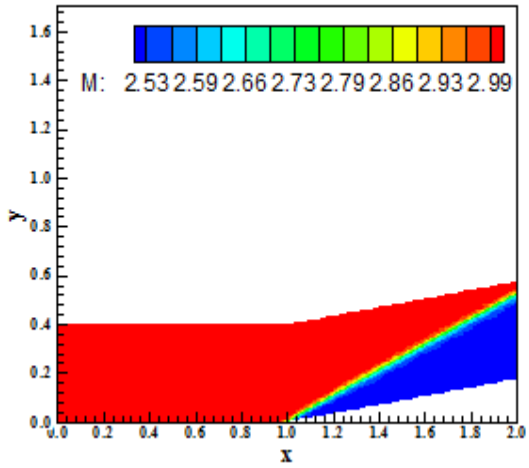


Figure 34. Mach number contours (VL-BJ).

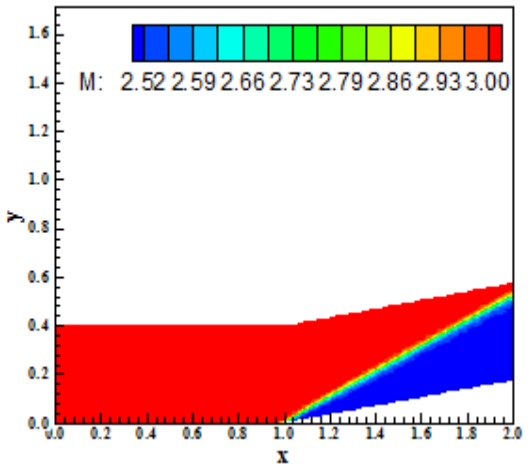


Figure 35. Mach number contours (VL-VL).

Figure 39 shows the wall pressure distributions generated by the five variants of the [2] algorithm. As can be observed, the AS case presents a smoothing of the pressure plateau,

eliminating the oscillation and peaks presents in the SS case. It is a remarkable feature of the AS case: due to its better symmetry properties, the solution is far more improved and better resolution is achieved. The best solution is obtained by the [2] scheme using the BL non-linear limiter.

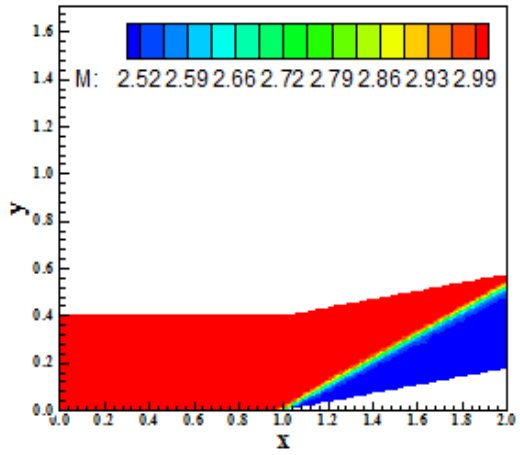


Figure 36. Mach number contours (VL-VA).

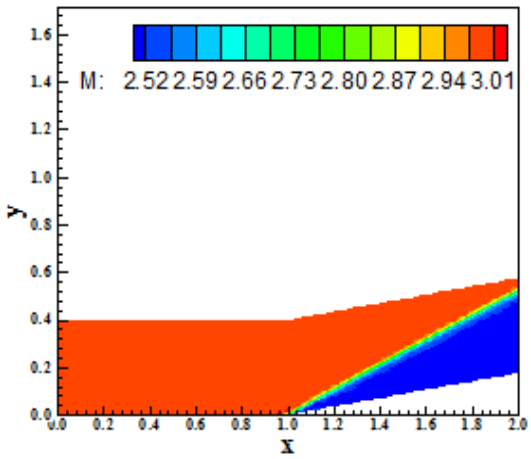


Figure 37. Mach number contours (VL-SB).

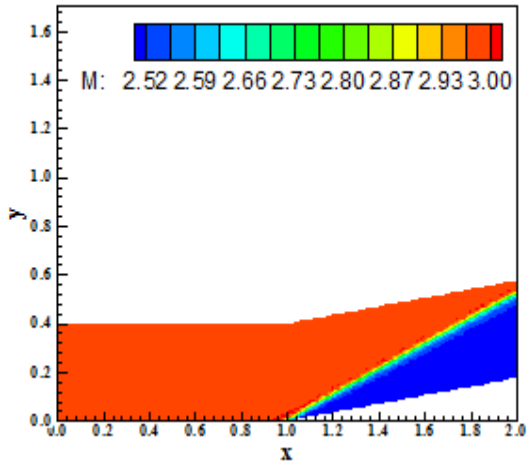


Figure 38. Mach number contours (VL-BL).

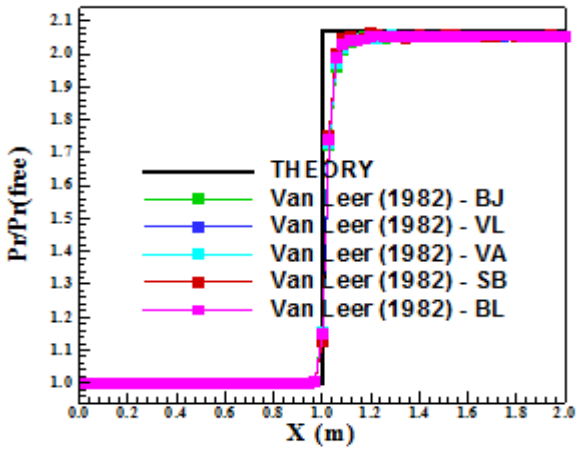


Figure 39. Wall pressure distributions (VL).

Table 3. Shock angle and percentage errors ([2]).

| Variant | β (°) | Error (%) |
|---|---|---|
| BJ | 27.9 | 1.45 |
| VL | 27.5 | 0.00 |
| VA | 27.6 | 0.36 |
| SB | 27.2 | 1.09 |
| BL | 27.0 | 1.82 |

Again, the shock angle of the oblique shock wave can be considered to quantitatively measure the level of accuracy that each variant of the [2] scheme presents for. Noting that again $\beta_{THEORETICAL} = 27.5°$, using a transfer in Figs. 29 to 33, one has in Tab. 3. The results highlight the [2] scheme, in its VL variant, as the most accurate of the studied versions, with an error of 0.00%.

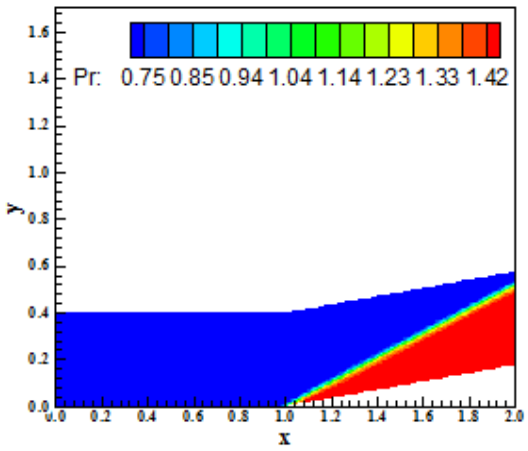


Figure 40. Pressure contours (RK-BJ).

Figures 40 to 43 exhibit the pressure contours obtained with the [4] algorithm in its four variants. The SB non-linear limiter did not present converged results. What is more important to note in these figures, is the notable improvement in the

solution quality of the pressure contours. Oscillations disappeared and shock wave thicknesses are thin. It is a very surprising characteristic of this procedure to solve unstructured Euler equations. As seen in [6,7], a great feature of this procedure had been in the viscous turbulent simulations, where the flow symmetry at the re-entry capsule's trailing edge had been guaranteed only because of the alternated sense in the mesh generation process. Now, it guarantees not only the homogeneity in the pressure and Mach number contours, but also corrects and yields the thinnest thickness of the shock wave, to both algorithms.

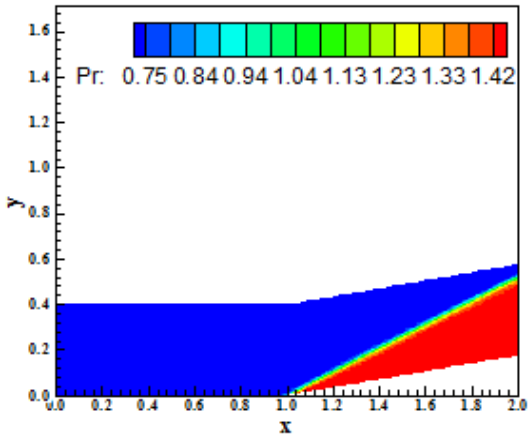


Figure 41. Pressure contours (RK-VL).

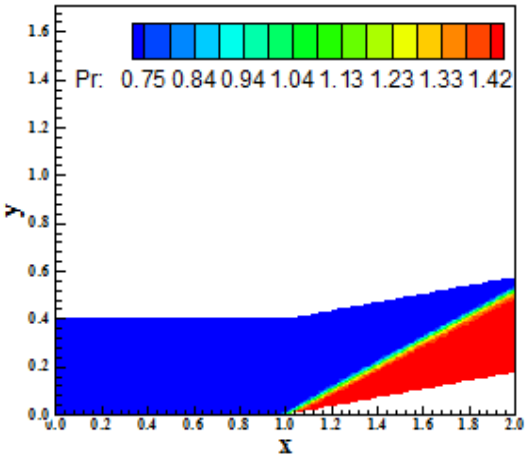


Figure 42. Pressure contours (RK-VA).

Figures 44 to 47 present the Mach number contours obtained by the algorithm of [4] in its four variants. As notable, the shock wave thickness is far thinner than in the respective solution in the SS case. A pre-shock oscillation occurred at the corner beginning in the BL solution, producing a non-homogeneity field close to the wall. All variants capture appropriately the shock wave at the corner.

Figure 48 shows the wall pressure distributions obtained by the [4] scheme. All variant's solutions are plotted. They are compared with the oblique shock wave theory results. An improvement is clear: the shock discontinuity was captured using three cells, which is very significant. The best pressure distribution is due to the VL variant.

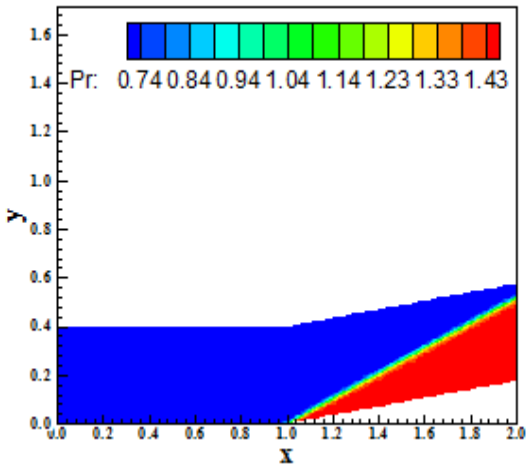


Figure 43. Pressure contours (RK-BL).

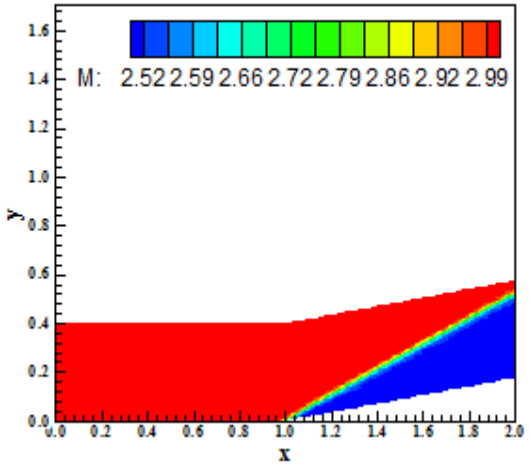


Figure 44. Mach number contours (RK-BJ).

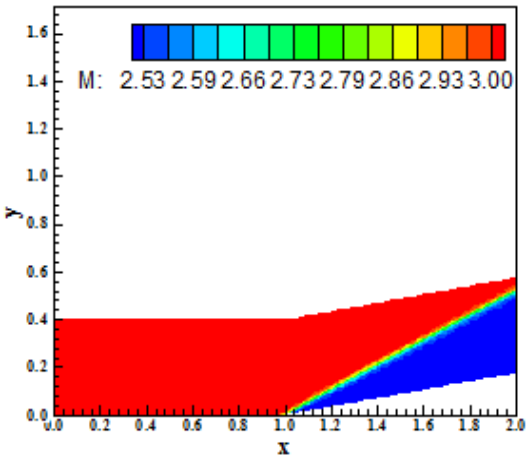


Figure 45. Mach number contours (RK-VL).

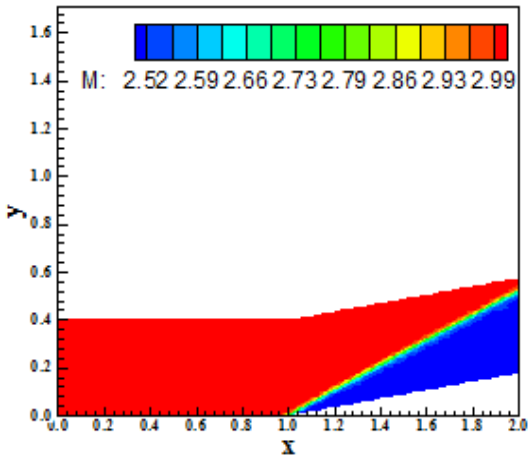


Figure 46. Mach number contours (RK-VA).

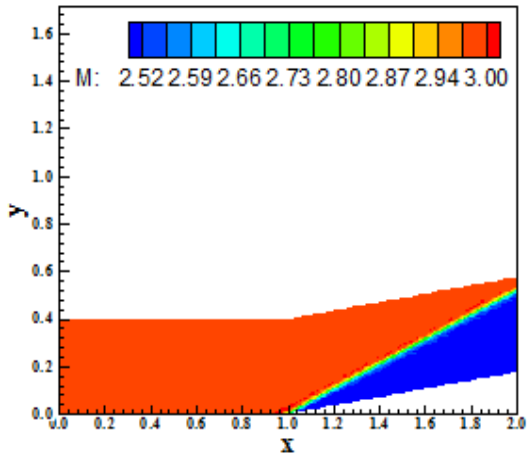


Figure 47. Mach number contours (RK-BL).

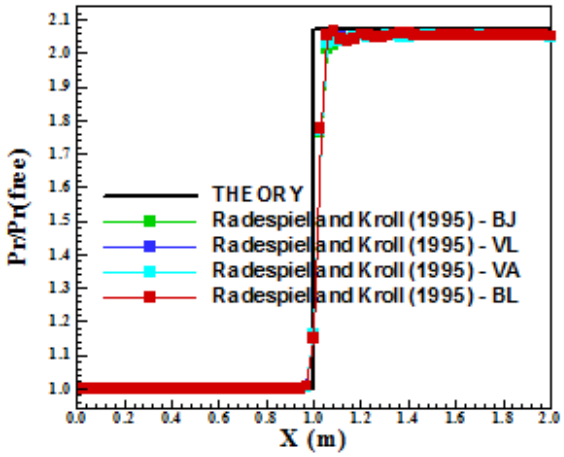


Figure 48. Wall pressure distributions (RK).

Again, the shock angle of the oblique shock wave can be considered to quantitatively measure the level of accuracy that each variant of the [4] scheme presents for. Noting that again $\beta_{THEORETICAL} = 27.5°$, using a transfer in Figs. 40 to 43, one has in Tab. 4:

Table 4. Shock angle and percentage errors ([4]).

| Variant | β (°) | Error (%) |
|---|---|---|
| BJ | 27.4 | 0.36 |
| VL | 27.0 | 1.82 |
| VA | 27.6 | 0.36 |
| BL | 27.1 | 1.45 |

The results highlight the [4] scheme, in its BJ and VA variants, as the most accurate of the studied versions. These non-linear limiters obtained the best solutions with an error of 0.36%.

### *C. Inviscid Conclusions*

In qualitative terms, the best solution was obtained by the [2] scheme using the BL non-linear limiter due to its best wall pressure distribution. In quantitative terms there are three variants that present the exact solution: VL – SS – SB, RK – SS – BL, and VL – AS – VL. As the qualitative results were good as the AS simulation was performed, the VL – AS – VL was chosen the best scheme to the quantitative results. Therefore, the [2] scheme, in its BL and VL variants, is the best scheme to the inviscid case studied in this work.

### *D. Turbulent Solutions – Same Sense Mesh Generation*

In this work, three turbulence models were studied: the k-ω model of [10], the k-ε and k-ω model of [11] and the k-ω model of the [12]. It is important to remember that the [11] turbulence model has four (4) variants: Wilcox, Two-Layers, BSL and SST. All these variants are studied in this work. Initially the SS case was considered.

*Re-entry capsule problem*

The re-entry capsule configuration is shown in Fig. 49, whereas the re-entry capsule mesh, generated in the SS case, is exhibited in Fig. 50. Three freestream Mach numbers were studied, each one related to the maximum value of this parameter that each model was able to support.

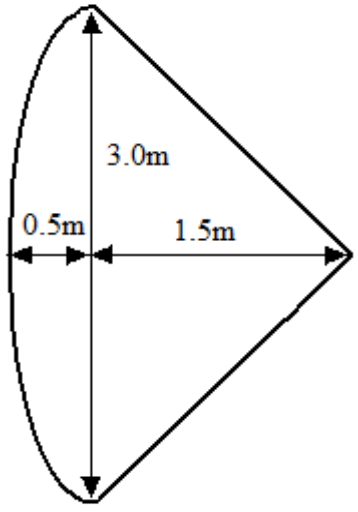


Figure 49. Re-entry capsule configuration.

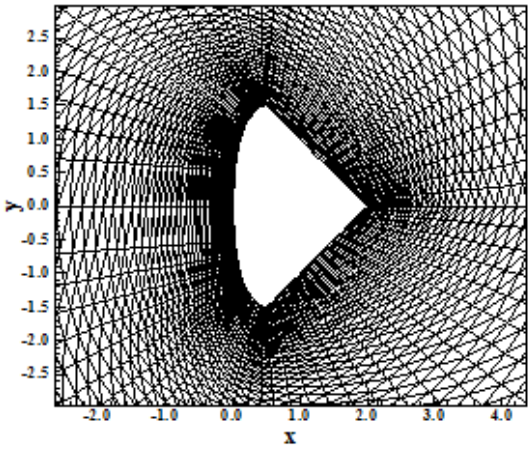


Figure 50. Re-entry capsule mesh (SS case).

Table 5. Freestream conditions to the re-entry capsule problem.

| Mach | Re | Mesh | Stretching | Model |
|---|---|---|---|---|
| 7.0 | $1.66 \times 10^6$ | 65x51 | 7.5% | W, MR, YGO |
| 9.0 | $2.14 \times 10^6$ | 65x51 | 7.5% | W, YGO |
| 11.0 | $2.61 \times 10^6$ | 65x51 | 7.5% | W |

Hence, in Table 5 is presented the test cases that were performed by the [2, 4] algorithms in the solution of this turbulent problem. Only first order solutions were obtained. The Reynolds number is also included in Tab. 5 to characterize the flow. For instance, for M = 7.0, all turbulence models simulated this problem; for M = 9.0, only the [10] and the [12] simulated this problem; and for M = 11.0, only the [10] simulated this problem. [23] gives the Reynolds number.

*Case 1 – M = 7.0 (Low "cold gas" hypersonic flow)*

Figures 51 and 52 exhibit the pressure contours obtained by the [2] and the [4] algorithms as using the [10] turbulence model. The pressure field generated by the [2] scheme is more strength than the respective field in the [4] scheme. Good symmetry properties are observed, even in the SS mesh generation procedure. Figures 53 and 54 present the Mach number contours obtained by each algorithm. As can be observed, a wake is formed in both solutions at the configuration trailing edge. Non-symmetry is noted at the wake, which is an indicative that the separation region behind the re-entry capsule geometry presents an unsymmetrical behavior. This consideration implies that the pair of circulation bubbles that is formed in this region is unsymmetrical too. In both solutions the maximum freestream Mach number exceeded the original freestream Mach number. It could be a problem of the algorithm or of the turbulence model under study. This aspect will be verified in the following sections.

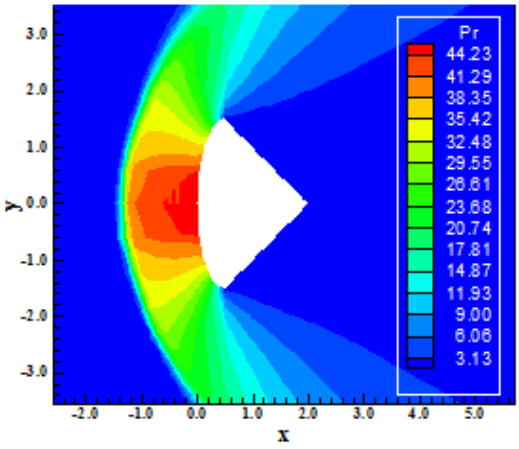


Figure 51. Pressure contours (VL-W).

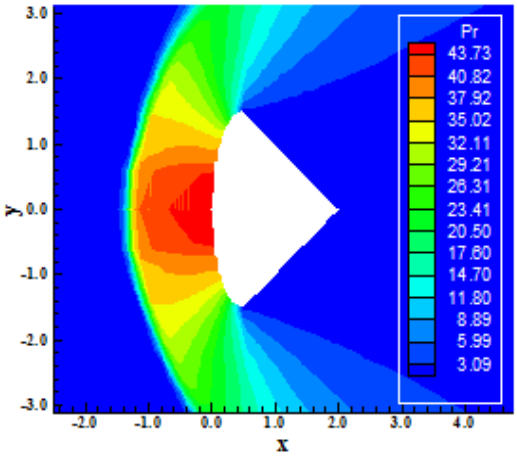


Figure 52. Pressure contours (RK-W).

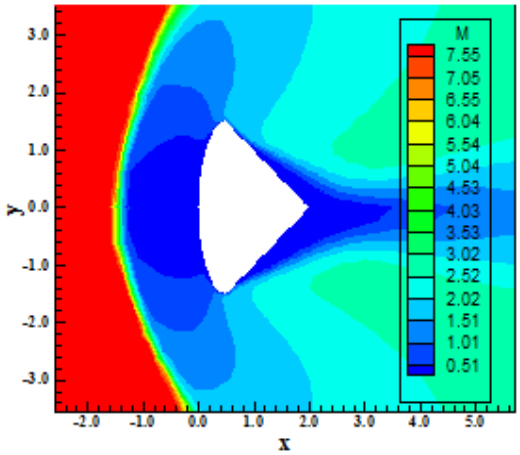


Figure 53. Mach number contours (VL-W).

Figures 55 and 56 exhibit the velocity vector field and the streamlines around the re-entry capsule configuration. Both solutions present good symmetry properties. The [4] solution presents a small non-symmetry characteristic at the trailing edge. Both solutions present a wake formed at the trailing edge

and this wake is not positioned at the body's symmetry line, indicating a non-symmetry zone. Afterwards it will be shown that it is characteristic of the mesh generation process and that the AS generation process eliminates this solution aspect. In general, the solutions are good.

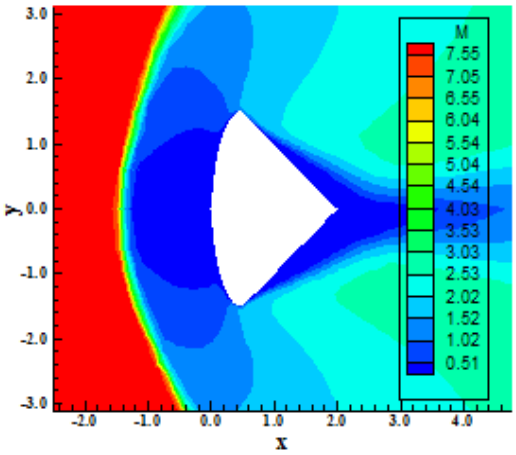


Figure 54. Mach number contours (RK-W).

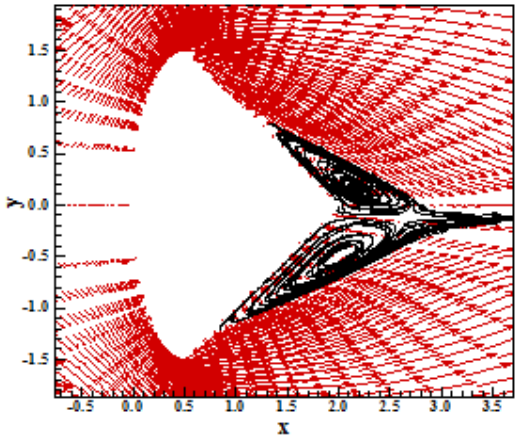


Figure 55. Velocity field and streamlines (VL-W).

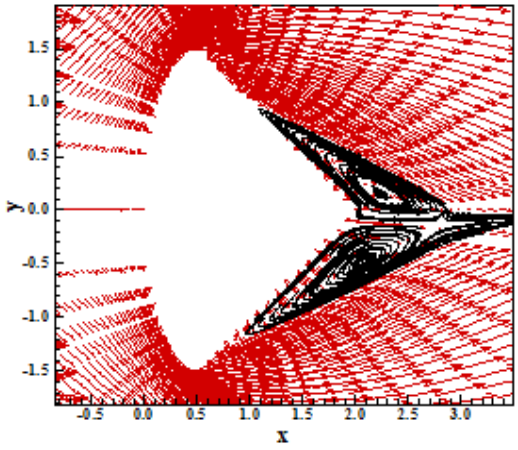


Figure 56. Velocity field and streamlines (RK-W).

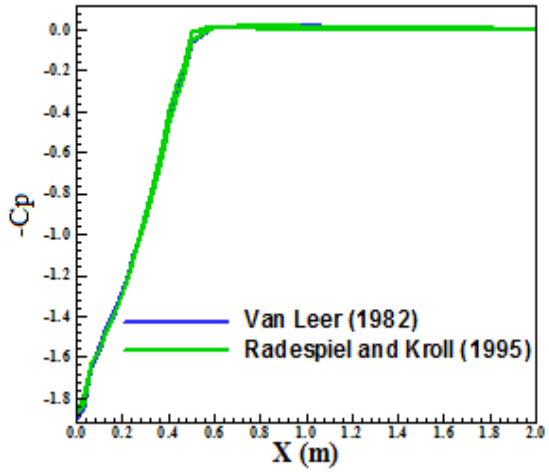


Figure 57. -Cp distributions at wall.

Figure 57 shows the wall pressure distributions obtained by the [2, 4] schemes, in terms of -Cp distribution. The solutions are very close, without meaningful differences. The -Cp plateau equal to zero indicates that at the separation region the pressure is constant and has its freestream value. In other words, in a region of great exchange of energy, the pressure is constant and equal to its freestream value. The Cp peak at the re-entry capsule leading edge is approximately 1.92 for both schemes. The variation of –Cp at the ellipse region is practically linear, without great variations. The Cp behavior, hence, is characterized by a linear region at the ellipse zone and by a constant region, with Cp = 0.0, at the linear zone of the re-entry capsule. This Cp behavior is typical of blunt nose bodies.

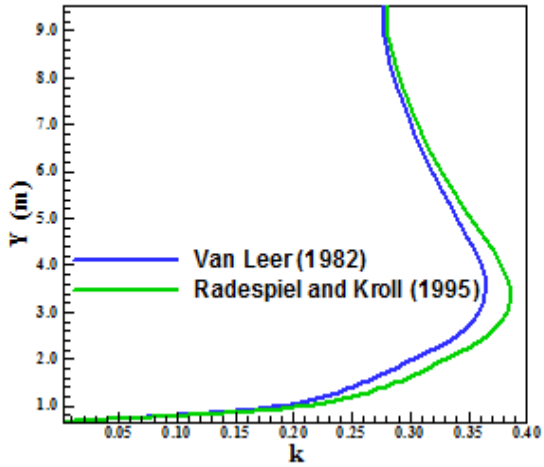


Figure 58. Turbulent kinetic energy.

Figures 58 and 59 exhibit the turbulent kinetic energy profile and the turbulent vorticity profile captured by the [2, 4] algorithms at node 58. As can be seen, the kinetic energy of the [4] scheme is bigger than the respective energy of the [2] scheme. It means that the [4] scheme remove more kinetic

energy of the mean flow than the [2] scheme does. In terms of vorticity, both schemes dissipate approximately the same quantity of energy. Note that the vorticity is maximum close to the wall.

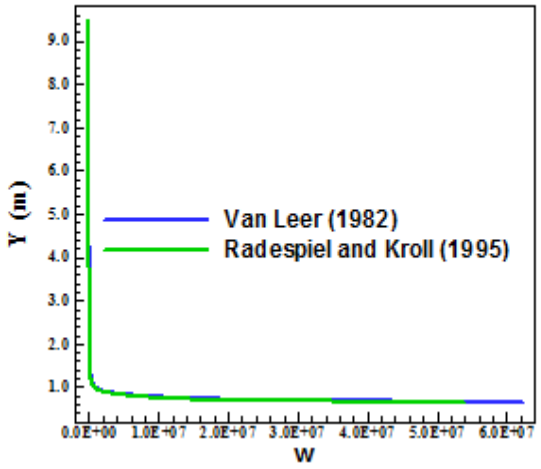


Figure 59. Turbulent vorticity.

Figure 60 shows the u distribution along y, respectively. The u profile presents a reverse flow close to y = 0.0 and characterizes as turbulent profile because of the large width close to the wall and a linear behavior approaching the boundary edge.

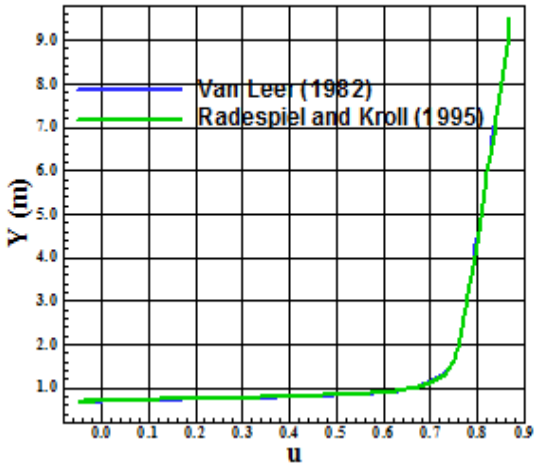


Figure 60. u profile.

## X. CONCLUSIONS

In this work, the third of this study, numerical simulations involving supersonic and hypersonic flows on an unstructured context are analysed. The [2, 4] schemes are implemented on a finite volume formulation, using unstructured spatial discretization. The algorithms are implemented in their first and second order spatial accuracies. The second order spatial accuracy is obtained by a linear reconstruction procedure based on the work of [8]. Several non-linear limiters are studied using the linear interpolation based on the work of [9]. To the turbulent simulations, the [10-12] models are employed. The compression corner problem to the inviscid simulations and the re-entry capsule problem to the hypersonic viscous simulations are studied. The results have demonstrated that the [2] algorithm yields the best results in terms of the prediction of the shock angle of the oblique shock wave in the compression corner problem and the best value of the stagnation pressure at the configuration nose in the re-entry capsule configuration. The spatially variable time step is the best choice to accelerate the convergence of the numerical schemes, as reported by [13-14]. In terms of turbulent results, the [10] model yields the best results, proving the good capacity of this turbulence model in simulate high hypersonic flows. This paper is continuation of Maciel's works started in 2011 and treats mainly the influence of turbulence models on the solution quality.

The forth part of this study will terminate the Mach number 7.0 studies and perform the consecutive analyses.

## REFERENCES

[1] P. Kutler, "Computation of Three-Dimensional, Inviscid Supersonic Flows", *Lecture Notes in Physics*, Vol. 41, pp. 287-374, 1975.

[2] B. Van Leer, "Flux-Vector Splitting for the Euler Equations", *Proceedings of the 8th International Conference on Numerical Methods in Fluid Dynamics*, E. Krause, Editor, Lecture Notes in Physics, Vol. 170, pp. 507-512, Springer-Verlag, Berlin, 1982.

[3] M. Liou, and C. J. Steffen Jr., "A New Flux Splitting Scheme", *Journal of Computational Physics*, Vol. 107, pp. 23-39, 1993.

[4] R. Radespiel, and N. Kroll, "Accurate Flux Vector Splitting for Shocks and Shear Layers", *Journal of Computational Physics*, Vol. 121, pp. 66-78, 1995.

[5] P. L. Roe, "Approximate Riemann Solvers, Parameter Vectors, and Difference Schemes", *Journal of Computational Physics*, Vol. 43, pp. 357-372, 1981.

[6] E. S. G. Maciel, "Supersonic and Hypersonic Flows on 2D Unstructured Context: Part I", *WSEAS Transactions on Fluid Dynamics*, Vol. 6, October, Issue 4, pp. 199-226, 2011.

[7] E. S. G. Maciel, "Supersonic and Hypersonic Flows on 2D Unstructured Context: Part II", *WSEAS Transactions on Fluid Dynamics*, Vol. 6, October, Issue 4, pp. 227-256, 2011.

[8] T. J. Barth, and D. C. Jespersen, "The Design and Application of Upwind Schemes on Unstructured Meshes", *AIAA Paper 89-0336*, 1989.

[9] F. Jacon, and D. Knight, "A Navier-Stokes Algorithm for Turbulent Flows Using an Unstructured Grid and Flux Difference Splitting", *AIAA Paper 94-2292*, 1994.

[10] D. C. Wilcox, "Reassessment of the Scale-Determining Equation for Advanced Turbulence Models", *AIAA Journal*, Vol. 26, No. 11, pp. 1299-1310, 1988.

[11] F. R. Menter, and C. L. Rumsey, "Assessment of Two-Equation Turbulence Models for Transonic Flows", *AIAA Paper 94-2343*, 1994.

[12] D. A. Yoder, N. J. Georgiadids, and P. D. Orkwis, "Implementation of a Two-Equation k-omega turbulence model in NPARC", *AIAA Paper 96-0383*, 1996.

[13] E. S. G. Maciel, "Analysis of Convergence Acceleration Techniques Used in Unstructured Algorithms in the Solution of Aeronautical Problems – Part I", *Proceedings of the XVIII International Congress of Mechanical Engineering (XVIII COBEM)*, Ouro Preto, MG, Brazil, 2005.

[14] E. S. G. Maciel, "Analysis of Convergence Acceleration Techniques Used in Unstructured Algorithms in the Solution of Aerospace Problems – Part II", *Proceedings of the XII Brazilian Congress of Thermal Engineering and Sciences (XII ENCIT)*, Belo Horizonte, MG, Brazil, 2008.

[15] F. R. Menter, "Zonal Two Equation k-ω Turbulence Models for Aerodynamic Flows", *AIAA Paper 93-2906*, 1993.

[16] B. E. Launder, and B. I. Sharma, "Application of the Energy-Dissipation Model of Turbulence to the Calculation of Flow Near a Spinning Disc", *Letters in Heat and Mass Transfer*, Vol. 1, No. 2, pp. 131-138, 1974.
[17] A. Jameson, and D. Mavriplis, "Finite Volume Solution of the Two-Dimensional Euler Equations on a Regular Triangular Mesh", *AIAA Journal*, Vol. 24, No. 4, pp. 611-618, 1986.
[18] D. J. Mavriplis, "Accurate Multigrid Solution of the Euler Equations on Unstructured and Adaptive Meshes", *AIAA Journal*, Vol. 28, No. 2, pp. 213-221, 1990.
[19] S. Pirzadeh, "Structured Background Grids for Generation of Unstructured Grids by Advancing Front Method", *AIAA Paper 91-3233-CP*, 1991.
[20] E. S. G. Maciel, "Simulação Numérica de Escoamentos Supersônicos e Hipersônicos Utilizando Técnicas de Dinâmica dos Fluidos Computacional", Ph.D. Thesis, ITA, CTA, São José dos Campos, SP, Brazil, 2002.
[21] P. L. Roe, In Proceedings of the AMS-SIAM Summer Seminar on Large-Scale Computation in Fluid Mechanics, edited by B. E. Engquist et al., *Lectures in Applied Mathematics*, (Amer. Math. Soc., Providence, R. I., 1985), Vol. 22, p. 163, 1983.
[22] J. D. Anderson Jr., *Fundamentals of Aerodynamics*, McGraw-Hill, Inc., 563p, 1984.
[23] R. W. Fox, and A. T. McDonald, *Introdução à Mecânica dos Fluidos*, Ed. Guanabara Koogan, Rio de Janeiro, RJ, Brazil, 632 p, 1988.